Korean Journal of Chemical Engineering (2024) 41:1551–1566
https://doi.org/10.1007/s11814-024-00159-5

REVIEW ARTICLE

Numerical Investigations of Collision Modes of Double Droplets on a Spherical Surface Based on the Phase Field Method

Changzhi Jiang[1,2] · Zhaohui Wang[1,2,3] · Qianwen Yang[1,2] · Quanjie Gao[1,2,3] · Deli Li[1,2]

Received: 29 November 2023 / Revised: 3 March 2024 / Accepted: 20 March 2024 / Published online: 3 April 2024

Abstract

Droplet collision on surface is widely existed in nature and industrial production. In our research, two-dimensional rotational models and three-dimensional symmetric models based on the phase field method have been developed to simulate the collisions of continuous droplets on spherical surfaces. Using parametric dimensionless, the spreading diameter of the coalescing droplets, the width of the liquid bridge between the droplets, and the moving velocity of the three-phase contact line are obtained. When the two droplets are coaxial, the collision velocity of the droplets increases, and the radial velocity of the liquid bridge also increases. Due to the increase of droplet energy, both the first and second maximum spreading are increased, but the characteristic spreading t_s time is reduced. When using the modified capillary inertia time τ_i' normalized spreading time t_s, it is found that it fits well with the Weber number (We) by the curve 1.505 $We^{-0.478}$. Increasing the ratio of curved surface to droplet diameter λ can reduce maximum spreading time and maximum rebound height of droplet. When there is a deviation between the centers of the droplets, the spread of the droplets no longer shows symmetry and the center of the condensed droplets moves towards the offset side of the tail droplets. These findings will provide insight into the dynamics of continuous droplet collisions.

Keywords Double droplet · Phase-field method · Impact · Neutral spherical surface · Spreading factor

Introduction

The coalescence impact of liquid droplets on solid walls, liquid films, and droplets is a common phenomenon, such as in the industrial field. Spray cooling technology on hot metal surfaces, the process of atomized fuel droplets hitting the cylinder block in the engine combustion chamber, and the high-speed collision between steam droplets and water film, steam droplets in the turbine. In nature, the collision of falling raindrops with the surface of a lotus leaf and the spreading of oil droplets on the surface of a fish scale. The impact of liquid droplets on solid walls has also been heavily applied and researched in agriculture [1, 2], industry [3–6], and forensic medicine [7], such as fuel combustion [8], aerospace [5], hydropower [6], and spray cooling [9]. This involves the diffusion properties of droplets, energy transfer, and satellite droplet generation. In agriculture, understanding the collision of pesticides on the surface of plant stems and leaves after spraying can help reduce the number of pesticides used per unit area. In industrial food coating, the quality of coating relies on the impact of the coating solution on the food surface during coating formation, as well as in daily life, where droplet collision and diffusion phenomena are present in the fall of water droplets and the formation of grease stains on clothing.

In nature and industry, the wall conditions for droplet impacts are usually not ideal but complex and variable. Therefore, more and more researchers have paid attention to droplet impacts on complex planes and found that the target geometry significantly affects the droplet impact dynamics [10–15]. The impact of a droplet on a wall normally has two major phases: expansion and contraction, with surface

✉ Zhaohui Wang
zhwang@wust.edu.cn

1 Hubei Key Laboratory of Mechanical Transmission and Manufacturing Engineering, Wuhan University of Science and Technology, Wuhan 430081, China

2 Key Laboratory of Metallurgical Equipment and Control Technology of Ministry of Education, Wuhan University of Science and Technology, Wuhan 430081, China

3 Hubei Longzhong Laboratory, Wuhan University of Technology Xiangyang Demonstration Zone, Xiangyang 441000, China

tension, viscous, and inertial forces dominating the process. Changing the droplet own characteristics [16, 17], wall properties [18–20], or environmental conditions [21, 22], such as droplet viscosity, surface tension coefficient, contact angle, and ambient pressure gravity conditions, can cause a variety of outcomes, including deposition, partial rebound, full rebound, and splash. In recent years, the reduction of droplet–liquid contact time in the design of hydrophobic materials and surfaces has gained favor among researchers. With the help of experiments and numerical simulations, Bange [23] et al. found that a droplet can rebound from a surface if the total energy at the maximum recoil of the droplet exceeds the initial surface and gravitational energy, and conversely, the droplet oscillates on the surface without rebounding. In addition, the authors present a state-distribution diagram that predicts the rebound and non-rebound of droplets at a contact angle $\theta = 155°$. Shen et al. [24] simulated the collision of a droplet on a raised superhydrophobic conical surface and found that the droplet could rebound rapidly. The observation of a 28.5% reduction in contact time when compared to a flat surface implies that the contraction phase is responsible for the reduction in contact time. Wang [25] investigated droplet rebound on different micro- and nanotexture. They verified that the structure with a high solid percentage must provide sufficient capillary pressure to withstand the impact pressure of the droplets when the size of the texture of the surface is lowered to the nanoscale level. As a result, the compact nanotexture effectively reduces the contact time and enables fast droplet rebound.

The research of droplet impact on a solid plane has been carried out extensively with the help of experiments, theoretical analysis, and computer simulations of various kinds. In contrast, the research of droplets on curved surfaces has received less attention. For experimental validation, Liang et al. [26] carried out impact experiments of heptane droplets on a wetted spherical surface. Because curved surfaces spread differently than flat surfaces, the droplet wetting area appears as a spherical cap. The contact surface dimensionless diffusion factor ($\phi = A_s/A_{drop}$) was invoked to quantitatively analyze the diffusion of droplets in the range of droplet Weber numbers We = 7–87 and curvature ratios $\omega = 0.09$–0.448. It is discovered that the variation of the curvature ratio ω does not have a significant effect on the droplets during the initial diffusion phase, and the spreading factors are almost the same. After the initial stage, the effects become more noticeable. In addition, the authors observe that the diffusion factor varies linearly with time for different ω, and propose a linear model between dimensionless time and the diffusion factor ϕ. To validate the linear model correctness, the authors performed additional experiments with ethanol droplets, which revealed comparable tendencies to heptane droplets. Banitabaei [27] experimentally studied the collision of liquid droplets with stationary spherical particles. Starting from We = 200, droplet impacts on hydrophobic surfaces result in the formation of a liquid film. The increase in wettability leads to a corresponding decrease in the duration of the impact process. Bakshi [28] also do research on the influence of spherical particles. In their work, the collisions of droplets with spherical targets of different diameters were studied. The thickness of the film on the sphere surface indicates that the dynamics is divided into three distinct stages: initial deformation, inertia-dominated, and viscous-dominated. The transition to the viscosity-dominated stage happens faster at low Reynolds numbers. The thinning process of the film slows as the spherical diameter grows and the residual thickness increases. Charalampous [29] studied the impact of droplets on spherical particles between Weber numbers between $92 \le We \le 1015$ and Ohnesorge numbers between $0.007 \le Oh \le 0.0089$. In the target-droplet diameter ratio R^* ($R^* = R_s/R_0$) in the range of $1.8 < R^* < 11.1$, in addition to the common deposition and splashing, another state was observed, in which the droplets formed a stable crown structure. The research focuses on medium and high Weber numbers and R^* is greater than 1.

In terms of simulation with the aid of computers, a variety of simulation methods are commonly used such as Lattice Boltzmann Method, Phase Field method, Level-Set, Volume of fluid method and coupling of the two. Zhang [30] used a high-density three-dimensional lattice Boltzmann model to simulate the process of liquid droplets impacting planar and spherical targets, and studied the effects of Reynolds number and target droplet size ratio on droplet flow dynamics. When the Reynolds number controlled by the velocity is increased, the film thickness profile collapses to a single curve in the first and second stages. When the Reynolds number is controlled by changing the viscosity, the rate of film thickness reduction slows down with increasing viscosity. Controlling for other factors by changing only the droplet size ratio, the rate of film thickness reduction slows as the size ratio increases. Shen et al. [10] used two-dimensional pseudopotential LBM to discuss the effects of size ratio, Weber number, and contact angle on the impact of a single droplet on a spherical target. The initial velocity plays an important role in impact dynamics. For hydrophilic surfaces, droplets gather at different speeds at the bottom, reducing wettability will increase the possibility of droplet splashing. However, the effect of viscosity changes on impact dynamics was not considered in Shen's [10] work. The effect of viscosity, gas-phase density and diameter on droplet impact on a sphere was investigated in the research of Banitabaei [31] in conjunction with the CLSVOF (coupled level-set and volume-of-fluid) approach. Larger droplet-to-sphere diameter ratios increased the impact time. As the viscosity μ decreases ($1\text{cp} < \mu < 350\text{cp}$), the intramembrane flow velocity decreases, which also leads to an increase in the

thickness of the lamellae on the sphere and the remaining film thickness. Malgarinos [32] used VOF and adaptive grid technology to report the impact of water droplets on spherical particles under constant temperature conditions. At lower Weber numbers and DTP numbers, droplets are more prone to partial or complete rebound. In addition, the research also found that for high Weber numbers (> 40) and low TPD (< 0.62), the average velocity of droplets leaving the particles after coating is 0.5 ~ 0.8 times the initial impact velocity. Yan Peng [33] developed a method that combines Level Sets and interface unit immersion boundaries. They studied the impact behavior of droplet Weber number $1 < We < 150$ and Ohnesorge number $Oh = 0.0831$ on spheres of different diameters ($2 < R^* < 10$). The results indicate that the size of the spherical target has a significant impact on the impact dynamics, especially when the size is very small, the droplet will fracture in the first backward stage. However, this research is limited to neutral surfaces with a contact angle of 90°. Zhu et al. [34] developed a method for immersing boundaries and numerically studied them in the range of medium Reynolds numbers (~ 103) and Weber numbers (25 ~ 400). The influence of diameter ratio on impact dynamics was evaluated, and the diffusion and contraction mechanisms of droplets were determined. Hong [35] et al. studied the impact of double droplets on a spherical liquid film using a coupled level set and VOF method. The results indicate that surface curvature, droplet diameter, impact velocity, droplet spacing, and liquid film thickness all have important effects on the flow and heat transfer performance of droplets. Du [36] studied the impact dynamics of five single liquid droplets on solid spheres of different diameters using the phase field method. For low viscosity droplets, expansion factor β With dimensionless time τ satisfy $\beta \propto \tau^{0.5}$. In capillary state, expansion factor β Scale is We^{α}. And the index α compared to diameter λ satisfy $\alpha = 0.20\lambda^{-0.75} + 0.28$. In the viscosity region, β Scale is Re^{b}, index $b = 0.19^{\lambda - 1.96} + 0.22$.

Based on the relevant literature we have reviewed, the impact of a single droplet on a flat surface was carried out by Worthington [37] as early as 1905. Researchers have been exploring droplets for more than 100 years, and have conducted deep and extensive studies of single droplet models. Until the last 20 years, with the rapid development of high-frequency camera technology and computer-aided technology, the droplet impact process is demonstrated in milliseconds or even microseconds. The rapid development of multi-droplet dynamics research has expanded the prospects for applications in industry. Research has focused on the dynamics of two droplet impact planes, liquid films, and tubular surfaces in frontal collisions, and some research has modeled the effects of droplet velocity, diameter, center distance, and other factors on the collision. Typically, in 3D printing of bone scaffolds, binder droplets impact the surface of spherical hydroxyapatite (HA) [38], and exploring the properties of inter-droplet dynamics will be helpful with improving the print quality. This article combines this practical application and selects the basic and common model in the multi-droplet model—the double droplet model. The remaining organizational parts are as follows: Sect. "Models and Methods" presents simulation and verification; Sect. "Results and Discussion" presents results and discussion; and Sect. "Conclusions" presents conclusions.

Models and Methods

One of the keys to simulating multiphase flow is to track and capture the two-phase interface. The phase field [39] method provides a way to model fluid interfaces as having preferred thickness. One of the advantages of the phase field method is that it allows the contact line of the droplet to move along the wetting surface without any treatment for stress singularity [40]. In addition, the phase field method has good numerical stability for simulating two-phase flow with high density ratio, and can truly reflect the influence of surface tension [41]. In this article, the finite element simulation software COMSOL Multiphysics 5.6 was used to establish two-dimensional rotational and three-dimensional axisymmetric models of droplet collisions, and the correctness of the models was verified. Use simple computational domains and structured grids to ensure high accuracy of the model [42].

Phase Field Theory

The simplest equation for the energy density function in the phase field method is given by the following equation:

$$f_{mix}(\varphi, \nabla\varphi) = \frac{1}{2}\lambda\left|\nabla_{\varphi}\right|^2 + f_0(\varphi) \tag{1}$$

In the above equation, $\frac{1}{2}\lambda|\nabla\varphi|^2$ is the energy density at the two-phase interface, $f_0(\varphi)$ is the free energy density, and f_{mix} is the two-phase mixed energy density. When there are only phase 1 and phase 2 in the cell, the phase variable $\varphi = \pm 1$, which is usually expressed by the following equation:

$$f_0(\varphi) = \frac{\lambda}{4\varepsilon^2}\left(\varphi^2 - 1\right)^2 \tag{2}$$

λ is the mixing energy density parameter and ε represents the capillary width of the interface between the two phases, which is usually half the size of the smallest cell.

By integrating the free energy density indeterminately into the computational domain, the free energy is expressed by the following equation:

$$F = \int_{\Omega} f_{mix} d\Omega \tag{3}$$

Ω is the spatial region of the simulation. The chemical potential G is defined as the variational derivative of the free energy with respect to the phase variable ϕ:

$$G = \frac{\delta F}{\delta \varphi} = f_0(\varphi) - \lambda \nabla^2 \varphi \tag{4}$$

Van der Waals assumes that the minimum free energy is possessed at the equilibrium interface. Therefore, the interface satisfies the equation for the chemical potential $G = 0$. For a one-dimensional (1D) interface, obtain the equation:

$$df_0(\varphi) = \frac{\lambda}{2} d\left(\frac{d\varphi}{dx}\right)^2 \tag{5}$$

Since $f_0(\pm\infty) = 0$ and $\frac{d\varphi}{dx}\Big|_{x=\pm\infty} = 0$, integration yields the following equation:

$$f_0(\varphi) = \frac{\lambda}{2}\left(\frac{d\varphi}{dx}\right)^2 \tag{6}$$

From the definition of the volumetric energy density, the equilibrium interface φ is defined:

$$\varphi(x) = \tanh\left(\frac{x}{\sqrt{2}\varepsilon}\right) \tag{7}$$

From Eqs. (6) and (7), we can obtain:

$$\sigma = \frac{2\sqrt{2}}{3}\frac{\lambda}{\varepsilon} \tag{8}$$

Governing Equations

Combined with Fick's law, the Cahn–Hilliard [43] equation is obtained as an evolution equation for the phase variable:

$$\frac{\partial \varphi}{\partial t} = \nabla \cdot (\kappa \nabla G) \tag{9}$$

κ is phase-field mobility. The Cahn–Hilliard equation can be used to model the formation of flow interfaces as well as the evolution and dissolution of diffusion-controlled phase fields.

In order to make the fluid at the two-phase interface smoother and the interface easier to capture, the viscosity and density are given by

$$\rho = \rho_1 \frac{1-\varphi}{2} + \rho_2 \frac{1+\varphi}{2} \tag{10}$$

$$\mu = \mu_1 \frac{1-\varphi}{2} + \mu_2 \frac{1+\varphi}{2} \tag{11}$$

where subscripts 1 and 2 denote the dispersed and continuous phases, respectively. The incompressible flow from the Navier–Stokes equations equation and the Cahn–Hilliard advection equation are:

$$\nabla \cdot u = 0 \tag{12}$$

$$\frac{\partial u}{\partial t} + (u \cdot \nabla)u = \nabla \cdot \left[-\frac{p}{\rho} I + \frac{\mu}{\rho}\left(\nabla u + (\nabla u)^T\right)\right] + \frac{1}{\rho} G \nabla \varphi \tag{13}$$

$$\frac{\partial \varphi}{\partial t} + u \cdot \nabla \varphi = \nabla \cdot (\kappa \nabla G) \tag{14}$$

where u, p are the velocity and pressure, respectively.

We define the velocity direction as the direction of the droplet vertically downward. The contact angle is the angle between the normal phase of the liquid and the surface at the three-phase contact line. The unit normal phase n can be calculated by the following equation:

$$n = n_w \cos\theta + t_w \sin\theta \tag{15}$$

where n_w and t_w are unit vectors in the vertical and tangential directions of the surface, respectively.

Validation of Numerical Models

In order to validate the 2D and 3D models, the impact of a single droplet on a spherical surface was simulated using a triangular mesh and a tetrahedral mesh, respectively. The validation refers to the experimental results of Zhu [34] and Bakshi [28], which were modeled with the same parameters for validation, respectively. As shown in Fig. 1a, the form of the droplet at different moments is basically consistent with the experimental form of Zhu et al. Droplet diameter D0 = 2.22 mm, sphere diameter Ds = 3 mm, Reynolds number Re = 1636, Weber number We = 17 and static contact angle θ = 95°. Similarly in Fig. 1b, the variation of dimensionless thickness h^* ($h^* = h/D_0$) with dimensionless time t^* ($t^* = tv/D_0$) for the present simulation maintains a similar trend with Bakshi's experimental data. Droplet diameter D0 = 2.6 mm, sphere diameter Ds = 3.2 mm, Reynolds number Re = 4806, Weber number We = 131, static contact angle $\theta = 160°$. Figure 1c, compares 16,628, 20,055, 31,625, 41,875 (minimum size 5e−4 mm, 2e−4 mm, 1e−4 mm, 0.8e−4 mm, respectively) at four different mesh counts with triangular mesh type. The results show that the change in the number of meshes did not have a significant effect on the numerical

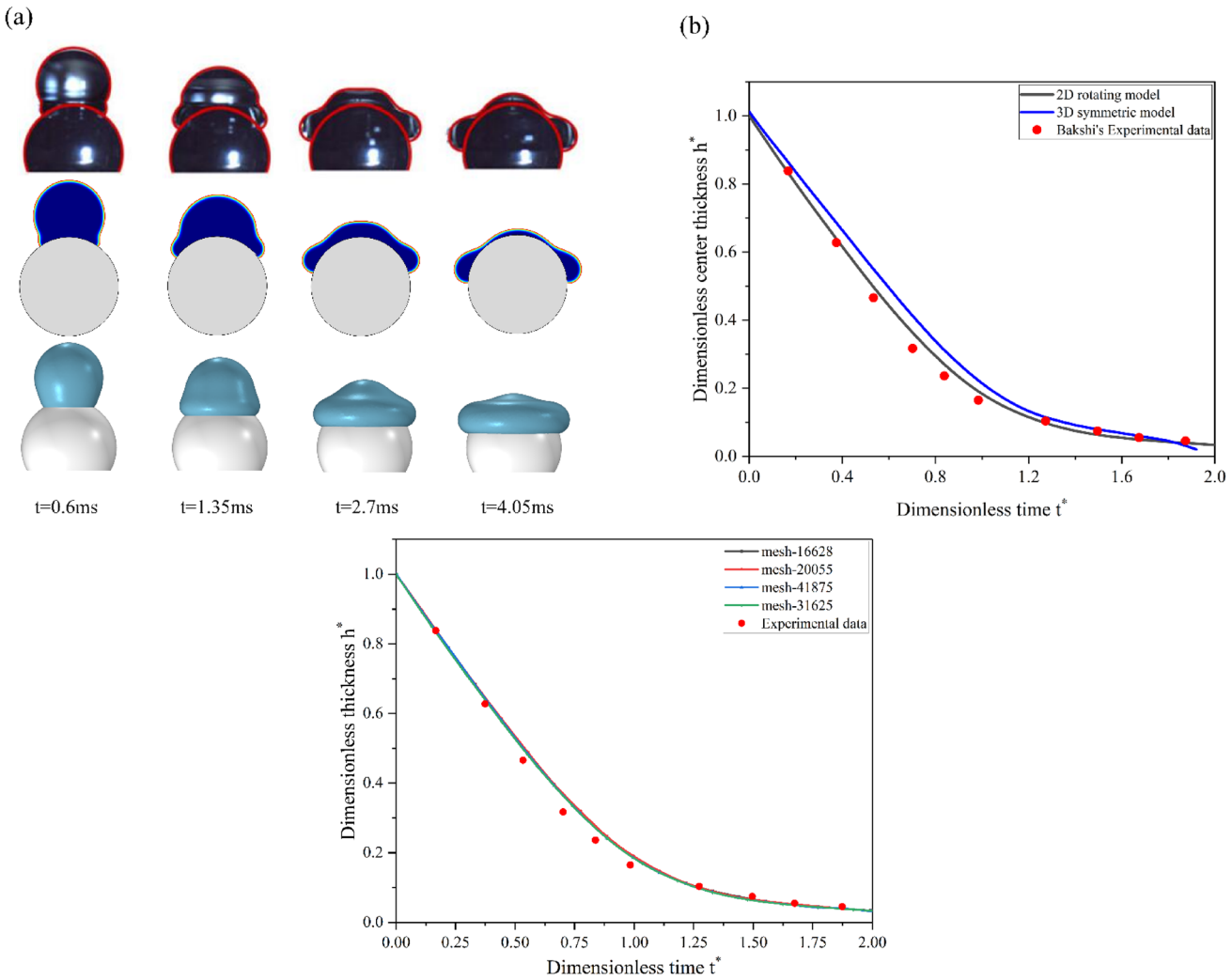

Fig. 1 **a** Comparison between simulation and experimental results for droplet morphology at a contact angle of 95°. **b** Comparison between simulation and experimental results on droplet thickness variation at a contact angle of 160°. **c** Results of grid independence validation under different grid sizes

simulation results, and we decided to use meshes with a minimum size of 1e−4 mm in the subsequent simulations.

Modeling and Boundary Conditions

The validation of the validity of the model has been completed in the previous sections, and we continue to discuss the kinetic process of the impact of a continuous droplet on a wall by discussing the effects of different factors on the impact process. The boundary conditions and initial conditions are shown in Fig. 2. The two droplets are located directly above the spherical surface and the point of impact is the highest point of the spherical surface. The droplets have the same radius $R_0 = 1$ mm and velocities v_1, v_2. The radius of the wetted spherical wall is $R_{ws} = 3$ mm and the offset distance is L^* $(= L/D_0)$. Open boundaries are set at the side and upper boundaries. The simulation space is a cylinder with a base radius of 5 mm and a height of 10 mm, with the center of the base as the origin of the coordinate system. In the meshing schematic Fig. 2c, the coarse mesh is a rectangular area of 2.5 mm*5 mm in the upper right corner, and the rest of the area is the fine mesh. In the research of Tang [44], the empirical correlation equation for droplet impact wall velocity was compared to Range [45] when air resistance was considered:

$$V_{im} = \sqrt{\left(\frac{g}{h}\right)\left(1 - e^{-2A(H-D_0)}\right)} \tag{16}$$

in the equation:

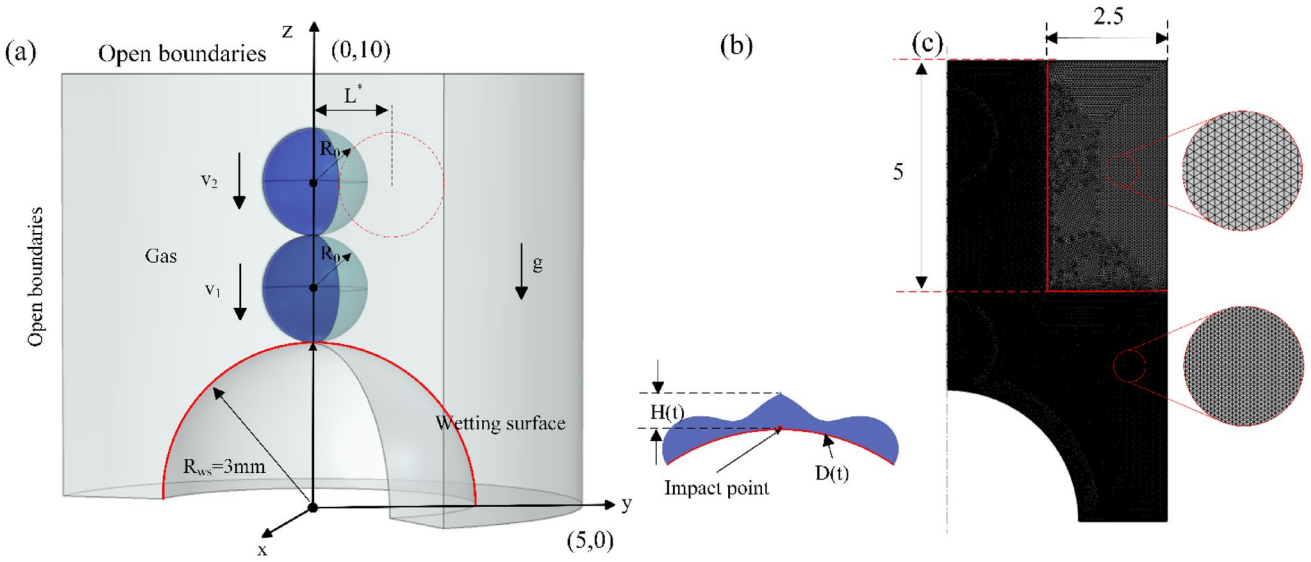

Fig. 2 **a** Numerical simulation area and boundary conditions; **b** schematic diagram of droplet spreading diameter and height on the spherical surface; **c** schematic diagram of local refinement of the mesh

Table 1 Physical properties of the liquid phase and gas phase

Material	ρ (kg/m^3)	μ (Pa · s)	σ (N · m)
Liquid	990	9e−4	0.069
Gas	1.204	1.814e−5	

$$A = \frac{3\rho_{air}C_f}{4\rho D_0} \tag{17}$$

when air resistance is not considered:

$$V_{im} = \sqrt{2g\left(H - D_0\right)} \tag{18}$$

Equations (16) and (18) where H is the initial height of the droplet, ρ_{air} is the air density, and C_f is the air resistance coefficient. When the droplet diameter is millimeter and H < 0.3 m, the air resistance has a negligible effect on the velocity of the droplet when it impacts the plane. While ensuring the accuracy of numerical simulation calculations, we reduce computational time and improve computational efficiency [46]. We adopt a differential partitioning method for the grid size of the computational domain. The collision region and non-collision region boundaries are virtualized as shown in Fig. 2 grid division. The droplet collision region uses an extremely refined mesh (number of meshes 91,343, minimum mesh size 1e-4 mm) and the non-collision region uses a generally refined mesh (number of meshes 32,442, minimum mesh size 7.5e−4 mm). We refer to the fluid properties used by Wang et al. [38] in the experiment for the gas–liquid two-phase properties, and the specific properties are shown in Table 1.

Results and Discussion

Effect of the Weber Number on Impact

In order to understand the effect of the impact velocity of the droplets on the impact dynamics, we change the velocities of the leading and trailing droplets by varying the droplet drop height, while their relative velocities are also changed. Figure 3 illustrates the sequence diagrams of the droplets during the impact on the sphere at three different Weber numbers We = 3.52/10/15 (v_1 = 0.35/0.59/0.72 m/s, v_2 = 0.29/ 0.56/0.7 m/s). When the leading droplet contacts the spherical surface, it spreads out rapidly, and the initial kinetic energy of the droplet is converted into surface energy, part of which is dissipated due to viscous forces. At around τ = 0.525, the leading droplet reaches its maximum spreading. Now, the droplet takes on a columnar shape, and its height becomes shorter as the relative velocity decreases. Subsequently, the edge liquid film keeps gathering to the center and the leading droplet undergoes a brief contraction. The trailing droplet merges with the leading droplet and keeps impacting downward inside the leading droplet. Under the impact of the trailing droplet, the center of the merged droplet sinks and spreads out again. When the coalesced droplet reaches maximum spreading, it presents a disc shape.

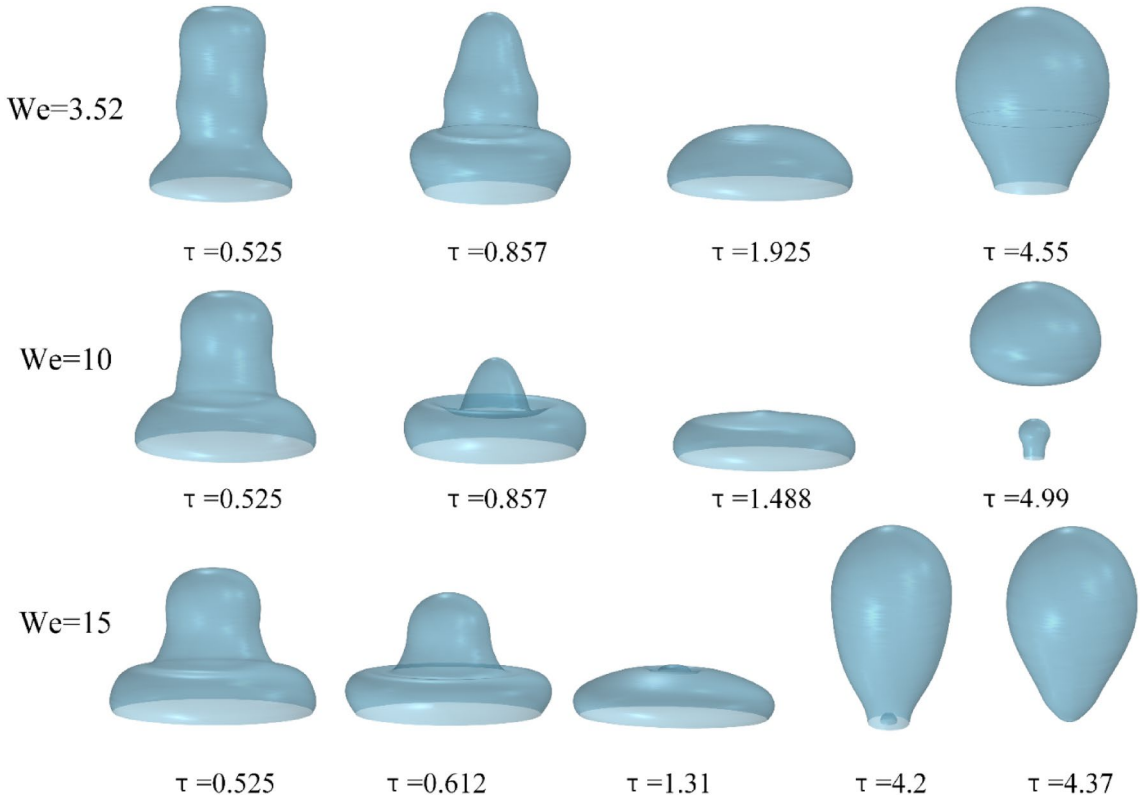

Fig. 3 Key frame sequence diagram of the droplet impact process at We = 3.52/10/15 (v_1 = 0.35/0.59/ 0.72 m/s, v_2 = 0.29/0.56/0.7 m/s)

Under the influence of surface energy, the coalesced droplet enters the contraction stage, and the liquid flows radially inward toward the center symmetry line. Because of the different initial kinetic energies of the droplet system, the three final outcomes are no rebound, partial rebound, and full rebound. The above spreading diameter D(t) and time t are dimensionlessized as follows:

Dimensionless spreading diameter:

$$\beta = \frac{D(t)}{D_0} \tag{19}$$

Dimensionless time:

$$\tau = \frac{tv}{D_0} \tag{20}$$

where $D(t)$ (unit: mm) for the moment t the actual spreading diameter of the droplet, D_0 for the initial diameter of the droplet, v (unit: m/s) for the initial velocity of the droplet.

Figure 4a illustrates the course of the spreading coefficient with time for different Weber numbers. The initial spreading process of the leading droplets does not seem to be affected by the Weber number, and there is no significant difference in the time to reach the maximum spreading $\beta_{max\text{-}1}$ around $\tau = 0.5$. However, the Weber number increased, the value of $\beta_{max\text{-}1}$ increased from 1.37 to 1.88 and the maximum spread $\beta_{max\text{-}2}$ increased from 2.02 to 2.86. The time interval $\Delta\tau$ between them has been shortened, which is related to the speed of the contact line movement of the droplets during spreading. $\beta_{max\text{-}1}$ and $\beta_{max\text{-}2}$ denote the maximum spreading factor that can be achieved by a droplet in the first spreading stage and the second spreading stage, respectively.

Figure 4b depicts the velocity change of the contact line during droplet spreading, and the inset shows a zoomed-in plot with time τ in the range of 0 ~ 2. At the instant when the leading droplet contacts the wall, the contact line has a large moving velocity, which decreases rapidly along with the spreading of the droplet. Near $\tau = 0.5$ and $\tau = 0.7$, the zero contact line velocity symbolizes that the droplet reaches the first and second maximum spreading. For droplets with lower Weber numbers We = 3.5 and We = 6, the contact linear velocity is significantly smaller than that of droplets possessing larger Weber numbers. A larger Weber number means that there is more energy within the droplet system, and more energy is available to overcome the viscous dissipation, thus more easily inducing the droplet to bounce off the wall.

When the leading droplet contacts the spherical surface, there is a relative difference in velocity between the two droplets, and liquid bridging occurs between the droplets due

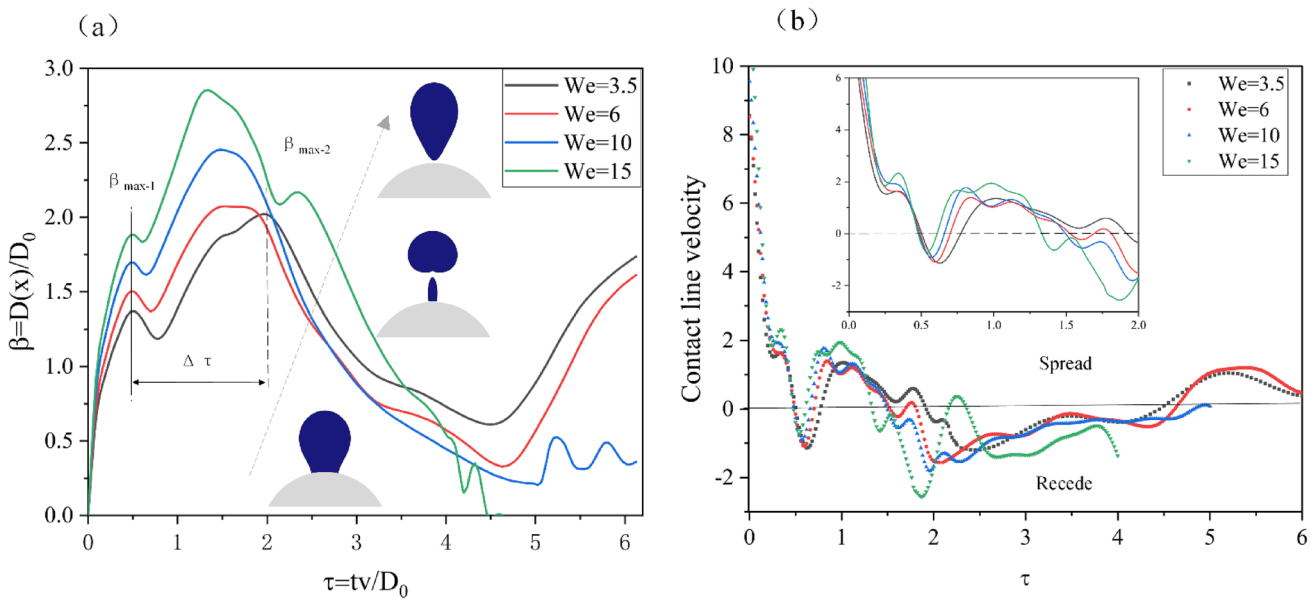

Fig. 4 **a** Variation of wetting diameter of droplets with time at different Weber numbers. **b** Variation of the moving speed of the three-phase contact line, the inset shows a localized magnification of the time in the range $0 \le \tau \le 2$

to inertia and capillary forces. Figure 5a shows the variation of the dimensionless width γ ($\gamma = D_b/D_0$) with time τ during the formation of the liquid bridge, which shows an overall increasing trend. Since the leading and trailing droplets possess a relative velocity difference at the contact instant, however, the increase of Weber number narrows the difference. It is maximum at We = 3.52 (0.061 m/s) and minimum at We = 15 (0.028 m/s). Therefore, when We = 3.52, the trailing droplet possesses greater relative inertia, and the liquid bridge expands outward more rapidly without changing the viscosity, also shortens the bridge formation time. Figure 5b, c compares the radial velocities of the liquid bridge as well as the surrounding capillary pressure for different Weber numbers in the numerical calculations. The results show that the radial velocity is larger at the beginning of the bridge construction and gradually decreases with time until the evolution of the liquid bridge is completed. Compared with other situations, the radial velocity of the liquid bridge decreases more significantly when We = 3.52, and the time to complete the evolution is also shorter. At the same time, we also found that in the early stage of coalescence, the capillary pressure is higher and gradually decreases over time. This is due to the very small width of the liquid bridge at the beginning of its evolution, which can cause higher external capillary forces ($P_c = 10^3 * \sigma/R_b$) decreases as the liquid bridge widens. The increase in the Weber number of droplets causes greater pressure on the external capillary.

Appendix Fig. 14 illustrates the 3D snapshots, velocity vectors and surface tension distributions of the liquid bridge formation at the same moment in time for three different Weber numbers. In the early stage of liquid bridge formation, the curvature at the bridge is large, forming a large surface tension and generating capillary waves on the liquid surface. As the width increases, the curvature of the liquid surface center soothes, and the region of high surface tension accompanied by capillary waves moves to the upper and lower sides. Velocity vector plots show that the edge droplets outside the leading droplets possess large relative flow velocities, and the fluid in the center of the coalescing droplets continues to flow downward. The merged droplet appears as a "dumbbell" with two large ends and a small center, which thickens as the droplet continues to collapse. At We = 3.52, time $t = 2.8$ ms, due to the small spreading speed of the leading droplet, the velocity difference between the two droplets is large, and the phenomenon of "bulging" occurs. This phenomenon still exists at We = 10, but with the increase of Weber number, the liquid bridge moves downward faster and the above phenomenon disappears. Compare the shapes of droplets reaching maximum spreading in different cases. In the low Weber number case, the inertial force of the droplet spreading outward is not enough to overcome the surface tension and it spreads out on the spherical surface in the form of a cake. In the high Weber number case, the droplets have a larger inertial force, and the droplets spread out on the spherical surface in a ring shape with a small number of droplets remaining in the center. After reaching the maximum spreading, the surface energy is converted into droplet kinetic energy and a small amount of viscous dissipation, and the droplets begin to recede. At low Weber number We = 3.52, rebound cannot occur because the energy

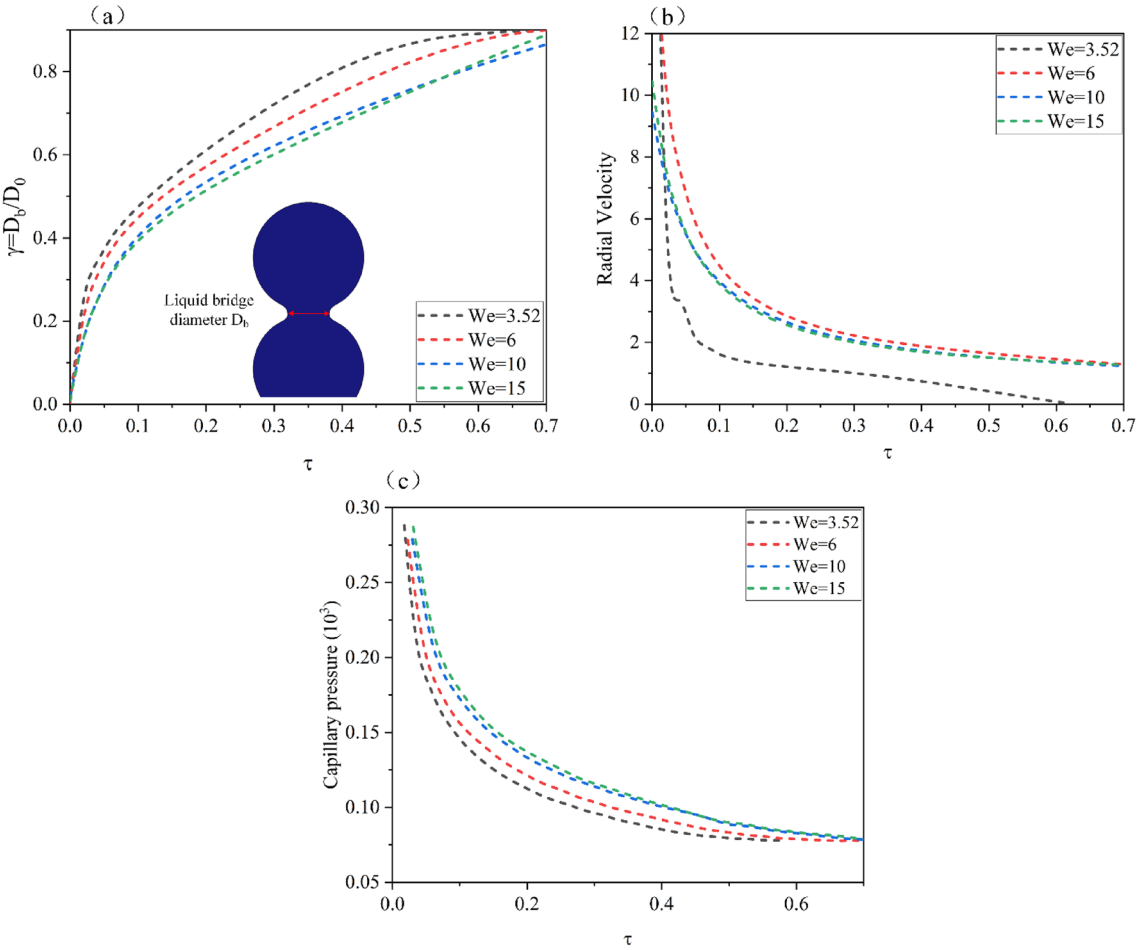

Fig. 5 Variation of dimensionless width of liquid bridge between two consecutive droplets D_b/D_0, radial velocity and external capillary pressure with time τ at different Weber numbers

of rebound is not enough to support the sum of the work done by surface tension and viscous forces, and eventually the droplet deposits on the spherical surface. At We = 10, the droplet is elongated, showing a large head and a small tail. At the liquid neck, it breaks into two parts under the shear effect of surface tension, with the smaller part staying on the spherical surface and the larger part rebounding. At We = 15, the droplet inertial force increases further and is sufficient to overcome the drag force and rebound completely from the spherical surface. The above shows that the increase in the Weber number of the droplet promotes the rebound of the droplet from the spherical surface, and there is a transition from deposition to partial rebound and eventually complete rebound.

Figure 6a plots the characteristic diffusion time on a spherical surface as a function of the Weber number for leading droplet velocities We = 1.15–15.71. The maximum spreading time is usually between a few milliseconds to a few tens of milliseconds. Within this interval, the maximum time t_s of the feature and the capillary inertia time τ_i ($= \sqrt{\rho R_0^3/\sigma}$) in the same order of magnitude. This means that the change in the velocity of the leading droplet is always dominant during the spreading and coalescence process. As shown in Fig. 6a, expand to $\beta_{max\text{-}1}$ The characteristic time t_{s-1} (black symbol) seems to be very stable under the change of Weber number, and there is no significant change. But expand to $\beta_{max\text{-}2}$ The characteristic time t_{s-2} (red symbol) is significantly influenced by the Weber number. The nonlinear changes indicate that droplets are influenced by various factors during the second stage of spreading and coalescence. In the range of We = 1.15 ~ 2.94, the characteristic time t_{s-2} variation decreases sharply. The opposite occurs between We = 3.51 ~ 7.17, where the t_{s-2} fluctuation rises, which again indicates that the aggregation between droplets is a very complex process. After We = 8.06, the characteristic time t_{s-2} gradually decreases with a slow decreasing trend, and after We = 12.12, it is in an overall smooth state. In the capillary inertia time normalized characteristic time t_s/τ_i in Fig. 6b, the variation trend is

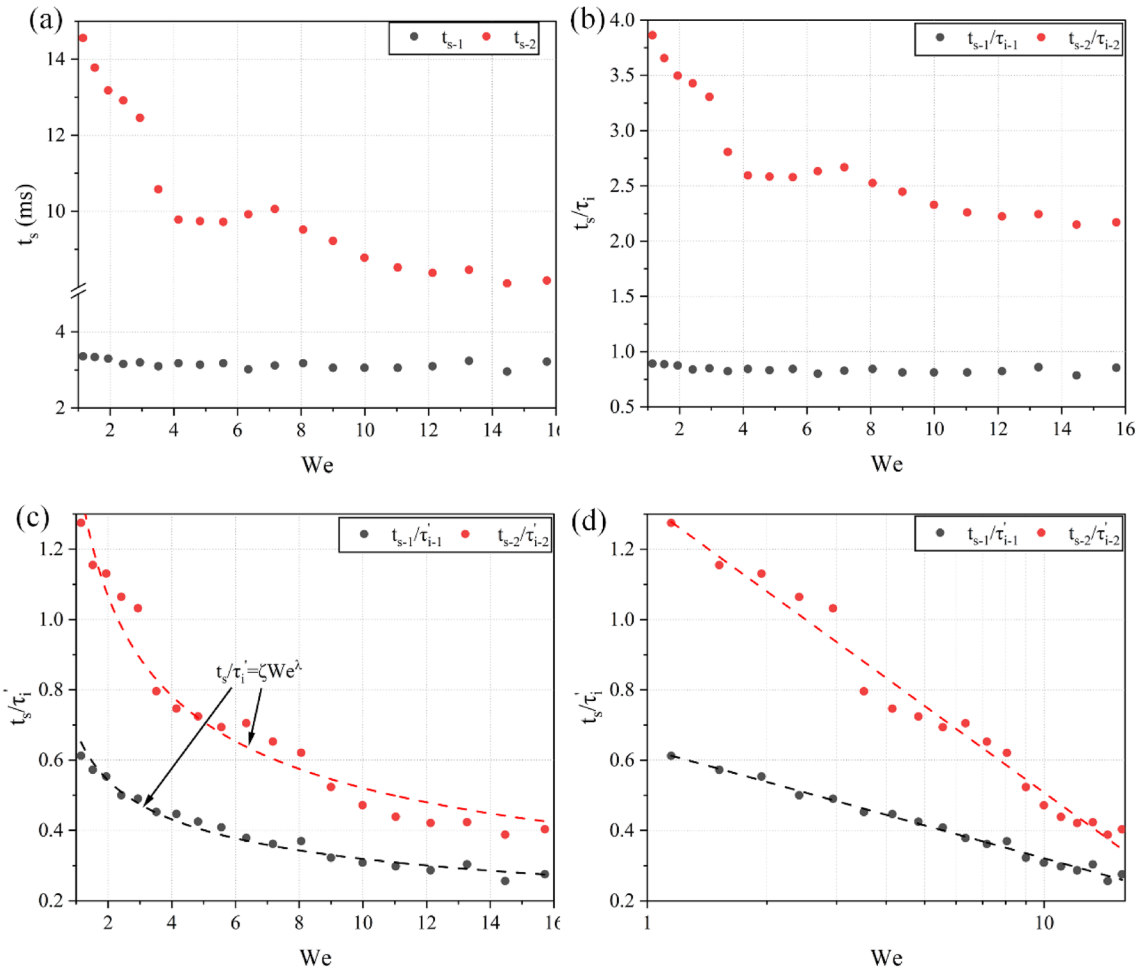

Fig. 6 **a** Feature spreading time t_s; **b** normalized feature spreading time t_s/τ_i; **c** modified normalized spreading time t_s/τ_i' as a function of the Weber number; **d** t_s/τ_i' conforms to the scaling law after modifying the transverse Weber number in **c** to a logarithmic scale

consistent with the characteristic time t_s because τ_i is a constant.

In Fig. 6a and b, it was observed that the characteristic time t_s is significantly affected by the Weber number, as the influence of velocity on the inertia time of the characteristic capillary is not taken into account. Therefore, we use the first and second maximum spreading factors determined by the Weber number $\beta/2$ replace capillary inertia time separately τ_i The initial radius R_0 of the droplet in is used to obtain the corrected capillary inertia time $\tau_{i-1,2}' = \sqrt{\rho\beta_{max-1,2}^3/8\sigma}$. As in Fig. 6c, both the first and the second spreads, after correction for the capillary inertia time τ' i normalized diffusion time $t_s/\tau_i' = \zeta W_e^{\lambda}$ were successfully fitted to a master curve. As shown in Fig. 6d, after replacing the horizontal and vertical coordinates with logarithms, the data is fitted into a straight line, indicating that the normalized spreading time of droplets on a spherical surface follows a power law. The convergence fitting curves in Fig. 6c are: $t_s/\tau_{i-1}' = 15.131We^{-0.235}$ and $t_s/\tau_{i-2}' = 1.505We^{-0.478}$, the majority of the residuals in the fitted curve are well distributed within the range of ± 8%, indicating good fitting performance. The above subscripts 1, 2 denote the first spreading stage and the second spreading stage, respectively.

Effect of Diameter Ratio on Impact

We investigated the effect of different diameter ratios λ ($\lambda = 2R_{ws}/D_0$) of continuous droplets on the impact process

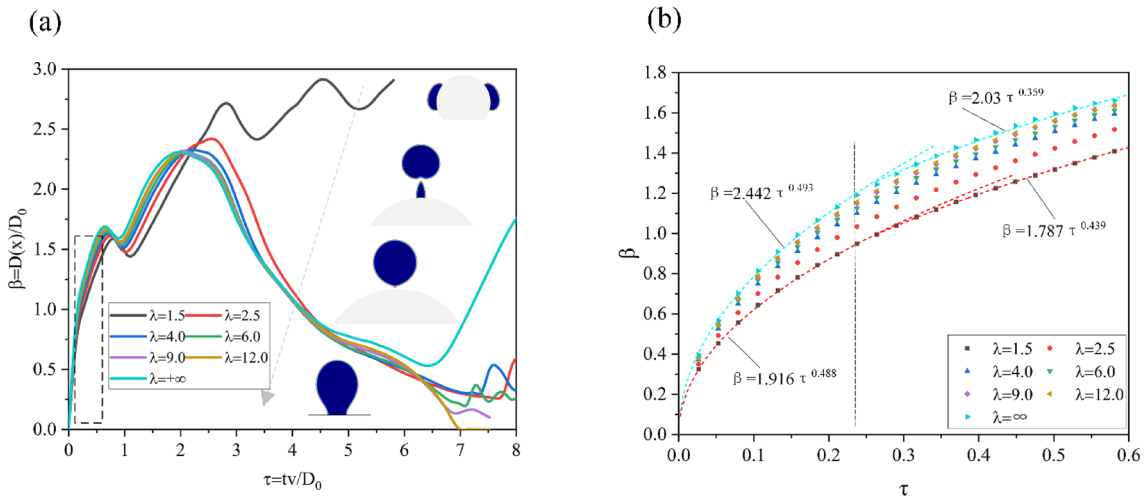

Fig. 7 **a** Variation of the spreading factor β for different diameter ratios λ, with $\lambda = +\infty$ denoting the plane; **b** In the kinematic phase ($0 < \tau < 0.1$), the spreading factor β can be fitted to a $\beta = a\tau^b$ curve

when the droplet We = 8, $\lambda = \infty$ Indicates that the wall is flat. Figure 7a shows the variation of the dimensionless diameter of the droplet with time. The spreading process of the droplet is divided into five stages: a kinematic stage, a spreading stage, a receding stage, a re-spreading stage and a re-contraction stage. This is because of the characteristic secondary spreading and receding of the droplet under the subsequent action of the trailing droplet, a phenomenon that also appeared in the previous section. When the droplet reaches $\beta_{max\text{-}2}$, it recedes under the action of surface tension. The change in curvature (diameter ratio λ) changes the dominant and strong effects of inertial, surface tension and viscous forces in the kinematics, resulting in different rebound outcomes. When λ = 1.5, the inertial force of the droplets plays a dominant role, overcoming the viscous force and surface tension, and sliding down from the top to the bottom of the spherical surface, with a continuous fluctuating rise in the spreading factor β. When λ = 4.0 ~ 12.0, the viscous force and surface tension effects are enhanced enough to overcome the inertial force and make the aggregated droplets work on the spherical surface.

The kinematic stage ($0 < \tau < 0.1$) of the leading droplet contacting the wall shows consistency in droplet spreading for different diameter ratios λ. For droplet collisions on a flat surface, the law $\beta \propto \tau^k$ ($0.45 < k < 0.57$) exists at kinematic stages [47, 48] which is also satisfied for single droplet collisions on a curved surface [36]. Figure 7b depicts the variation of the wetting diameter of a continuous droplet during the kinematic stage. The spreading factor β versus time τ satisfies $\beta = 1.916\tau^{0.488}$ when $\lambda = 1.5$, and $\beta = 2.422\tau^{0.493}$ when $\lambda = +\infty$. The fitted curves can well describe the spreading during the kinematics stage and the period of time afterward, and β is distributed in the middle of the two fitted curves for

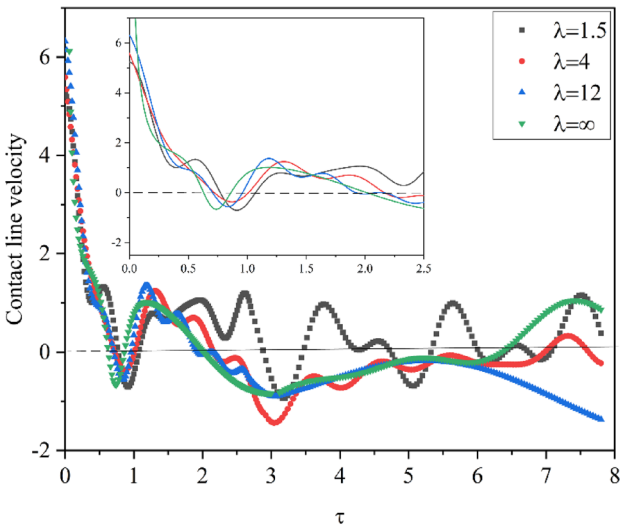

Fig. 8 Effect of diameter ratio on contact line travel speed, where the inset is a localized magnification in the range of time $0 \le \tau \le 2.5$

different λ. With time, near τ = 0.24, the droplet spreading tendency gradually deviates from the kinematic stage. It is observed in Fig. 8 that the contact linear velocity decreases continuously, after the first drop to zero, and again after a short recede. Throughout the impact process, the contact linear velocity of the droplet is relatively flat on the surface with diameter ratio λ = 12, $\lambda = \infty$, and it continues to oscillate and change on the surface with diameter ratio λ = 1.5, λ = 4.

In terms of the maximum spread diameter β_{max} (i.e., $\beta_{max\text{-}2}$) and the time to reach it. As shown in Fig. 9, when λ = 2.5, the agglomerated droplet has the maximum

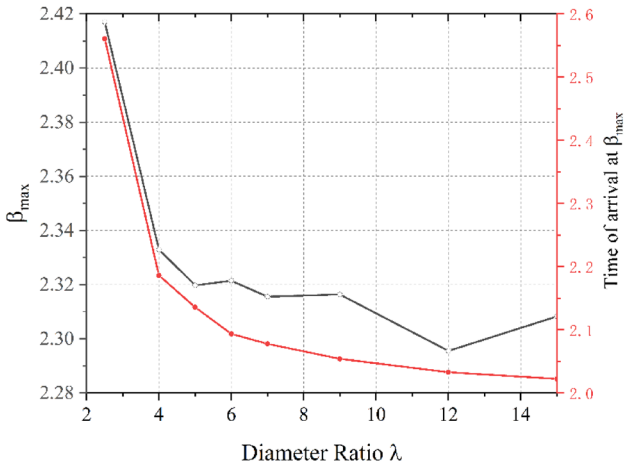

Fig. 9 Maximum spreading factor β_{max} and time to reach it for droplets at different diameter ratios λ

spreading diameter $\beta_{max}=2.4$, and the time to reach β_{max} $\tau=2.56$. When the diameter ratio λ is increased, the curvature of the wall surface decreases, and the viscous force between the droplet and the wall surface dominates the spreading process, and the energy used for the viscous dissipation of the droplet increases. Both the maximum β_{max} and the time to reach it decrease rapidly, and the droplet can reach the maximum spread more quickly. When the diameter ratio λ is increased to a certain point, the effect of the influence on the spreading phase is no longer significant and the maximum spreading β_{max} no longer changes significantly.

After reaching β_{max}, the droplet starts to recede under the effect of surface tension. Figure 10a shows the variation of the maximum rebound height h^* and the time to reach it for droplets with different diameter ratios λ. The increase in diameter ratio decreases the energy used by the droplet for rebound. The maximum rebound height h^* is 3.51 for the diameter ratio $\lambda=2.5$, and it decreases as the diameter ratio increases. In the range $2.5\leq\lambda\leq7$, h^* decreases more significantly than in the range $\lambda>7$. Regarding the contact time, for $2.5\leq\lambda\leq7$, the contact time decreases from $\tau=7.29$ at $\lambda=2.5$ to $\tau=6.89$ at $\lambda=7$. Subsequently, for $\lambda\geq7$, the contact time does not decrease further with the increase in diameter and seems to remain relatively constant.

Effect of Lateral Offset on Impact

In order to characterize the effect of offset distance on the spread of a continuous droplet on a spherical surface, dimensionless spreading diameter of the droplet in the transverse and longitudinal directions, described as follows:

$$\beta_x^* = \frac{S_x}{D_0}, \beta_y^* = \frac{S_y}{D_0} \tag{21}$$

where S_x and S_y are the actual spread of the droplets on the spherical surface in the yz and xz sections, respectively, as depicted in Fig. 11:

In order to better describe the collision process, a three-dimensional symmetric model is used that is distinct from the previous section. Appendix Fig. 15 depicts the evolution of continuous droplets on a spherical surface at four different offset distances, namely $L^*=0.05$, 0.15, 0.3, and 0.4. We can see that in all non-zero offset cases, the merging of droplets becomes asymmetric on the wall. The increase in offset distance means that the distance between the center of gravity of the droplet and the impact point increases, and the tail droplet exacerbates the asymmetry of the impact. At $\tau=1$, at this point, the trailing droplet has partially fused with the leading droplet. The tilting of the trailing droplet becomes more pronounced under surface tension at $L^*=0.3$, 0.4. In all cases, the final spread of the coalescence droplets

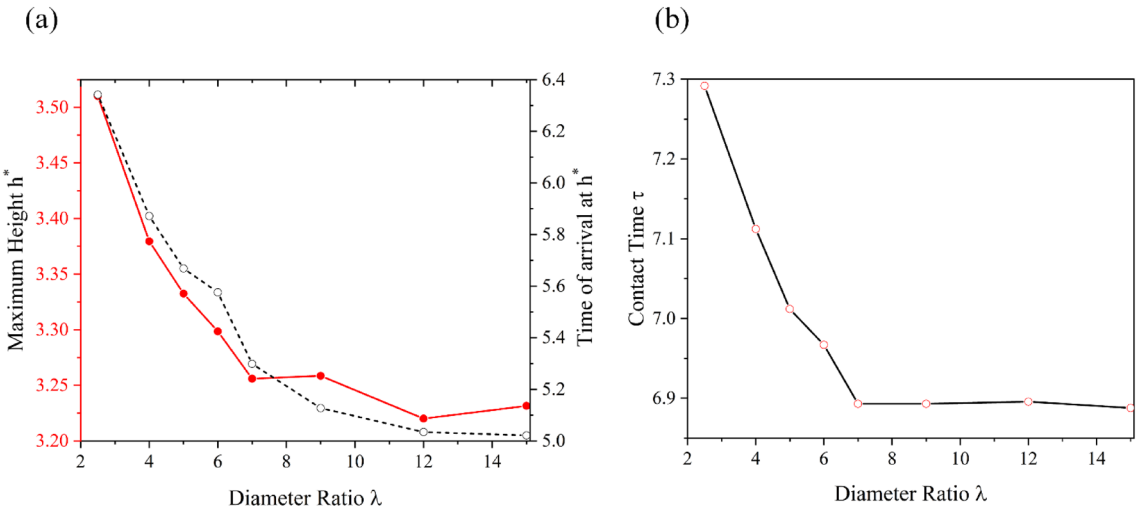

Fig. 10 Maximum rebound height h^* and contact time of droplets for different diameter ratios λ

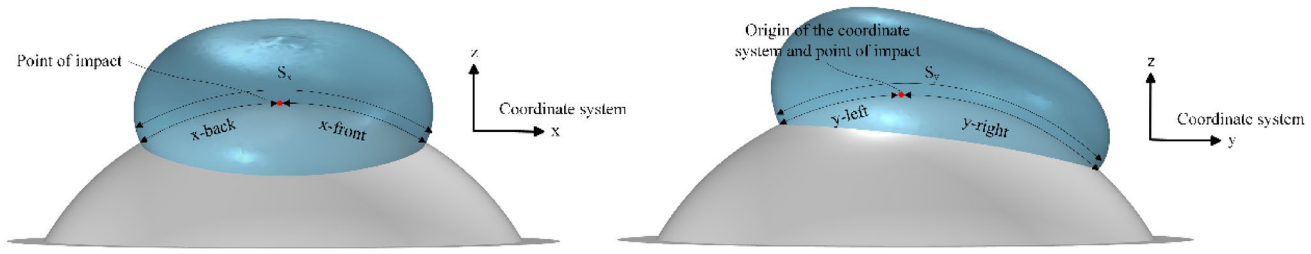

Fig. 11 Schematic diagram of dimensionless spreading distances of a continuous droplet in the *x* and *y* directions under non-zero offset conditions

on the spherical surface showed an annular shape. Due to the variation of the offset distance, the thickness of the liquid film on the left side of the liquid ring gradually becomes thicker under the impact of the trailing droplets. The $\tau = 3 \sim 7$ droplet is in the rebound stage, and in the case of low L^*, the droplet resembles a tilted cylinder. Because of the increase of L^*, the relative moving speed difference between the left and right contact lines increases, and the right contact line moves slower. In the case of high L^*, there is a bulge on the left side of the droplet and the whole is more of a triangular shape. Note that in the three cases of $L^* = 0.15$, 0.3 and 0.4, the left contact line briefly crosses the highest point of the spherical surface to reach the right side, and the droplet as a whole is on the right side of the sphere, a difference that we can obtain from the movement of the contact line in Fig. 13**.**

We show the trajectory of the droplet's center of gravity during rebound in the top region of Appendix Fig. 15. The coordinate origin is the impact contact point. We intuitively observe that the motion trajectory of the center of gravity changes most sharply at $L^* = 0.05$, and at the same time, the span in the *y*-axis direction is the narrowest. As the offset distance increases, the rise of the center of gravity becomes smooth and the span in the *y*-axis direction becomes wider. The maximum rise height of the center of gravity under the droplet inertial force and the curvature of the spherical surface also decreases. We can predict that the droplet may eventually slip out of the spherical surface as the offset distance increases further.

Figure 12 shows the evolution of the three-phase contact lines in the anterior–posterior (*x*) and left–right (*y*) directions of the coalescence droplet for the four cases, with the case of no offset ($L^* = 0$) added as a comparison. As can be seen in Fig. 12a, the fringe motion in the anterior–posterior direction does not break the symmetry of the motion due to the presence of offsets. The first maximum expansion of the contact line is reached at $\tau = 0.8$, and after a short period of recede it continues to spread until the maximum. In comparison to the no offset, the maximum spread in the non-zero offset case decreases with increasing L^*. The droplet reaches its maximum spread near $\tau = 2.64$ and then starts to recede. The droplets cross the impact point at $\tau = 5.94$, 6.02, and 6.73 for offsets $L^* = 0.15$, 0.3, and 0.4, respectively. Correspondingly, we observe at the end of the motion in Fig. 12c that the curves intersect the straight line $y/D0 = 0$, implying that at this point the contact lines all move to the right side. In Fig. 12b, the longitudinal expansion factor β_x^* in the anterior–posterior direction has a similar trend at different offsets *L*, with the maximum value generally decreasing with increasing L^*.

The evolution of the contact line on the left and right sides is compared in Fig. 12c, while the moving speed of the contact line is depicted in Fig. 13a, b. From Fig. 12c, it can be observed that in the early stage of the motion ($\tau = 0 \sim 0.6$), the wetting diameters and contact line moving velocities are the same for different L^*, indicating that the trailing droplet does not intervene in the motion of the leading droplet at this time. As time passes, the two droplets continue to merge and the difference in spreading diameter begins to appear. The increasing of L^*, the trailing droplet keeps moving away from the impact point, which makes the wetting diameter of the right side keep getting larger and the opposite left side keep getting smaller. The maximum β_y^* in Fig. 12d shows an increasing trend with increasing L^*. In the moving velocity diagram of the contact line in Fig. 13a, b. After reaching the first maximum spread, the left contact line has a larger recede than the right, and the larger the offset L^* the larger the recede in this stage. In the subsequent second spreading stage, the velocity of the contact line on the right side is larger than that on the left side, and the larger L^* is the larger the spreading velocity in this stage.

Conclusions

In this work, the effects of different Weber numbers, liquid-spherical diameter ratios and offset distances on the impact of continuous droplets are investigated based on a neutral spherical surface with a fixed contact angle ($\theta = 90°$). The phase field method (PF) is used to establish two-dimensional rotating and three-dimensional symmetric models, simulate the evolution of droplet impact process, and verify the correctness of the simulation model and the mesh independence. The research will provide theoretical analysis in the

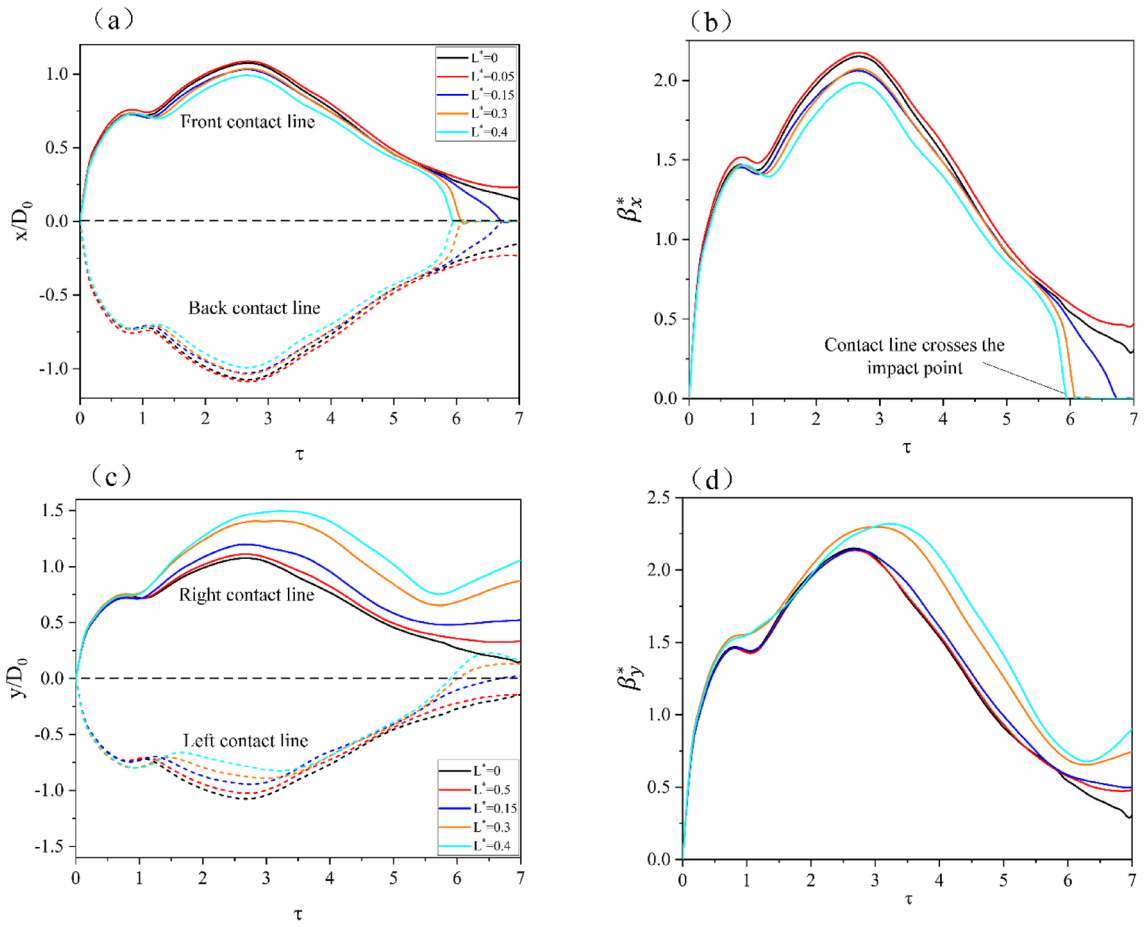

Fig. 12 Evolution with time τ of **a** front and back boundaries, **b** longitudinal expansion coefficients β_x^*, **c** left and right boundaries, and **d** transverse expansion coefficients β_y^*

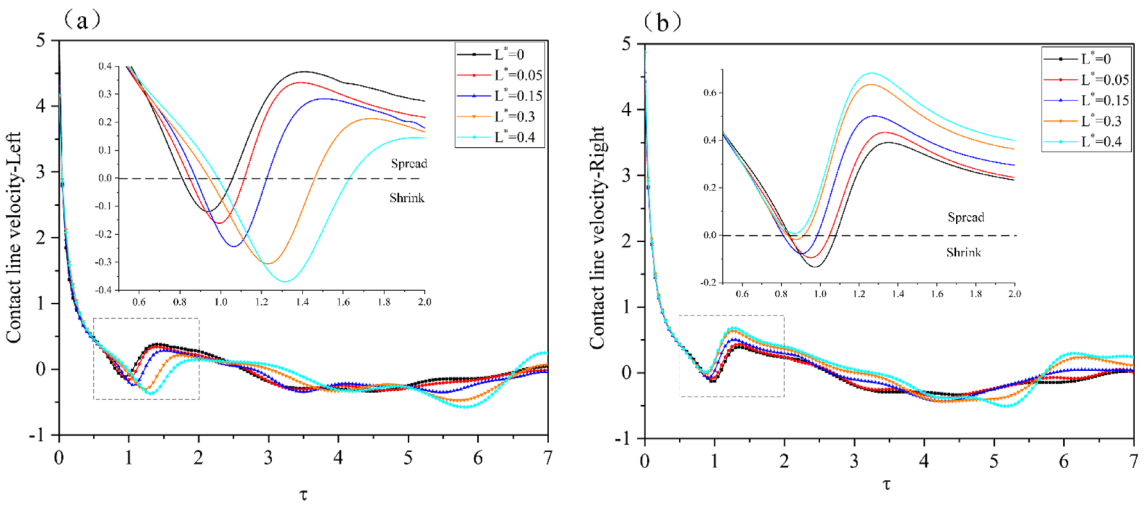

Fig. 13 In the transverse (*y*) direction. **a** Evolution of the moving speed of the right contact line; **b** evolution of the moving speed of the left contact line

field of 3D bone scaffold printing. The important findings of the research are as follows:

1. The collision process of two neighboring droplets was simulated for different Weber numbers ($3.5 \le We \le 15$). The knotted droplet undergoes two successive spreading and contraction. As the Weber number increases, the maximum spreading $\beta_{max\text{-}1}$ of the first stage of the droplet increases from 1.37 to 1.88, and the maximum spreading $\beta_{max\text{-}2}$ of the second stage increases from 2.02 to 2.86. The time interval $\Delta\tau$ between the two is shortened from 1.41 to 0.97. After correcting the capillary inertia time τ_i' using the first and second maximum spreading diameters $\beta_{max\text{-}1,2}/2$ and normalizing the characteristic diffusion time t_s, t_s/τ_{i-1}' can be fitted by the curve 15.131 $We^{-0.235}$ and t_s/τ_{i-2}' can be fitted by the curve 1.505 $We^{-0.478}$. The data were fitted to a straight line after the horizontal coordinate was transformed to logarithmic.
2. When varying the diameter ratio λ of the droplet to the sphere, the spreading factor β satisfies the $a\tau^b$ law in the early stage of kinematics ($0 < \tau < 0.1$) and is distributed in the middle region sandwiched between curves $\beta = 1.916\tau^{0.488}$ and $\beta = 2.422\tau^{0.493}$. The increase in the diameter ratio λ decreases the maximum spreading factor β from 2.41 to 2.29, and the maximum rebound height from 3.51 to 3.22, indicating that the increase in the diameter ratio increases the energy dissipation.
3. After the two droplets are no longer coaxial but have an offset distance, the spreading process in the y-axis direction no longer exhibits symmetry. As the offset distance L^* increases, the maximum contact line spreading factor in the y-axis direction decreases from 1.075 to 0.82 on the left side and increases from 1.075 to 1.496 on the right side. The total spreading factor on the *y*-axis increases from 2.15 to a large 2.31. The spreading factor decreases in the *x*-axis direction, but more noticeably than that, the increase in the diameter ratio accelerates the time it takes for the contact line to cross the vertex of the sphere.

Supplementary Information The online version contains supplementary material available at https://doi.org/10.1007/s11814-024-00159-5.

Acknowledgements We gratefully acknowledge the support of the National Natural Science Foundation of China (No. 51875419), the Independent Innovation Projects of the Hubei Longzhong Laboratory (2022ZZ-14) and the Open Foundation of the State Key Laboratory of Fluid Power and Mechatronic Systems (No. GZKF-202122).

Data availability The data that support the findings of this study are available within the article.

References

1. B. Majhy, V.P. Singh, A.K. Sen, JCIS **565**, 582 (2020)
2. J.W. Adams, T.R. Butts, D.M. Dodds, Weed Technol. **33**, 66 (2019)
3. C. Chen, J. Huang, H. Yi, Y. Zhang, J. Mech. Sci. Technol. **34**, 3197 (2020)
4. S. Wei, H. Jin, H. Zhou, K. Yang, N. Gao, W. Li, AIP Adv. **9**, 6 (2019)
5. N. Chen, J. Du, Y. Hu, H. Ji, Y. Yuan, AIP Adv. **10**, 4 (2020)
6. Z. Zhao, H. Li, A. Li, W. Fang, Z. Cai, M. Li, X. Feng, Y. Song, Nat. Commun.Commun. **12**, 6899 (2021)
7. C.D. Adam, Foren. Sci. Int. **303**, 109934 (2019)
8. H. Cong, L. Qian, Y. Wang, J. Lin, PhFl **32**, 10 (2020)
9. L. Prince-Raj, K. Yee, R.S. Myong, Aerosp. Sci. Technol.. Sci. Technol. **98**, 105659 (2020)
10. S. Shen, F. Bi, Y. Guo, IJHMT **55**, 6938 (2012)
11. L. Deng, H. Wang, X. Zhu, R. Chen, Y. Ding, Eng. Appl. Comput. Fluid Mech **12**, 598 (2018)
12. H. Chen, X. Liu, K. Wang, H. Liu, S. Shen, IJCFD **33**, 222 (2019)
13. S. Ahmad, H. Tang, H. Yao, IJHMT **119**, 433 (2018)
14. D.-J. Lin, L.-Z. Zhang, M.-C. Yi, X. Wang, S.-R. Gao, Coatings **10**, 6 (2020)
15 S.Y. Hitoshi-Fujimoto, K. Takahashi, T. Hama, Exp. Therm. Fluid Sci. **81**, 136 (2016)
16. P.G. Bange, G. Upadhyay, N.D. Patil, R.J.P.O.F. Bhardwaj, AIP Adv. Adv. **34**, 11 (2022)
17. M. Kumar, R. Bhardwaj, K.C. Sahu, PhFl **32**, 1 (2020)
18 T.D. Bonn, Phys. Rev. Fluids **6**, 043604 (2021)
19. L. Wang, X. Li, X. Kong, J. Feng, X. Peng, Eur. J. Mech. B. Fluids **96**, 146 (2022)
20 A.L. Xing, B.J. Li, C.M. Jiang, D.L. Zhao, PhFl **34**, 072114 (2022)
21 S. Farzana, R. Baily, P.R. Waghmare, Exp. Therm Fluid Sci **128**, 110450 (2021)
22. C. Xie, J. Zhang, V. Bertola, M. Wang, J. Colloid Interface Sci. **463**, 317 (2016)
23. P.G. Bange, R. Bhardwaj, ThCFD **30**, 211 (2015)
24. Y. Shen, S. Liu, C. Zhu, J. Tao, Z. Chen, ApPhL **110**, 221601 (2017)
25. L. Wang, R. Wang, J. Wang, T.-S. Wong, Sci. Adv. **6**, 29 (2020)
26. G. Liang, Y. Guo, X. Mu, S. Shen, Exp. Therm Fluid Sci **55**, 150 (2014)
27. S.A. Banitabaei, A. Amirfazli, PhFl **29**, 6 (2017)
28. S. Bakshi, I.V. Roisman, C. Tropea, PhFl **19**, 3 (2007)
29. G. Charalampous, Y. Hardalupas, PhFl **29**, 10 (2017)
30. D. Zhang, K. Papadikis, S. Gu, Int. J. Therm. Sci. **84**, 75 (2014)
31. S.A. Banitabaei, A. Amirfazli, PhFl **32**, 3 (2020)
32. I. Malgarinos, N. Nikolopoulos, M. Gavaises, IJHFF **61**, 499 (2016)
33. L. Yan-Peng, W. Huan-Ran, Can. J. Chem. Eng. **89**, 83 (2011)
34 Y. Zhu, H.-R. Liu, K. Mu, P. Gao, H. Ding, X.-Y. Lu, JFM **824**, 388 (2017)
35. W. Hong, Y. Wang, Numer. Heat Transfer, Part B **71**, 359 (2017)
36 Y. Du, J. Liu, Y. Li, J. Du, X. Wu, Q. Min, Colloids Surf. Physicochem. Eng. Aspects **625**, 126862 (2021)
37. H. Deka, G. Biswas, S. Chakraborty, A. Dalal, PhFl **31**, 1 (2019)
38. Y.-E. Wang, X.-P. Li, C.-C. Li, M.-M. Yang, Q.-H. Wei, JMatS **50**, 5014 (2015)
39. D. Jacqmin, JCoPh **15**, 1 (1999)
40. C.Y. Lim, Y.C. Lam, Microfluid. Nanofluid.. Nanofluid. **17**, 131 (2013)
41 Z. Wang, S. Dong, M.S. Triantafyllou, Y. Constantinides, G.E. Karniadakis, JCoPh **397**, 108832 (2019)

42. J.J. Feng, C. Liu, J. Shen, P. Yue, Model. Soft Matter **141**, 1 (2005)
43. J.W. Cahn, J.E. Hilliard, J. Chem. Phys. **31**, 688 (1959)
44. P.-B. Tang, G.-Q. Wang, L. Wang, Z.-Y. Shi, Y. Li, J.-R. Xu, AcPSn **69**, 2 (2020)
45. K. Range, F. Feuillebois, JCIS **203**, 16 (1998)
46. H. Liu, PhFl **31**, 9 (2019)
47. A. Gupta, R. Kumar, Comput. Fluids. Fluids **39**, 1696 (2010)
48. R. Rioboo, M. Marengo, C. Tropea, ExFl **33**, 112 (2002)